

High-impedance surface-acoustic-wave resonators

Yadav P. Kandel¹, Suraj Thapa Magar¹, Arjun Iyer,² William H. Renninger,² and John M. Nichol^{1,*}

¹*Department of Physics and Astronomy, University of Rochester, Rochester, New York 14627, USA*

²*The Institute of Optics, University of Rochester, Rochester, New York 14627, USA*

(Received 21 June 2023; revised 13 December 2023; accepted 14 December 2023; published 8 January 2024; corrected 2 February 2024)

Because of their small size, low loss, and compatibility with magnetic fields, and elevated temperatures, surface acoustic wave (SAW) resonators hold significant potential as future quantum interconnects. Here, we design, fabricate, and characterize gigahertz-frequency SAW resonators with the potential for strong capacitive coupling to nanoscale solid-state quantum systems, including semiconductor quantum dots. Strong capacitive coupling to such systems requires a large characteristic impedance, and the resonators we fabricate have impedance values above 100Ω . We achieve such high impedance values by tightly confining a Gaussian acoustic mode. At the same time, the resonators have low loss, with quality factors of several thousand at millikelvin temperatures. These high-impedance resonators are expected to exhibit large vacuum electric field fluctuations and have the potential for strong coupling to a variety of solid-state quantum systems.

DOI: 10.1103/PhysRevApplied.21.014010

I. INTRODUCTION

Interconnects play a key role in classical information processors and will likely play a similarly important role in large-scale quantum information processors [1,2]. Among the different types of potential quantum interconnects, mechanical resonators stand out for their desirable properties, including low loss, small size, and ability to couple to nearly all quantum devices [3–7]. Piezoelectric mechanical resonators can directly interact with other quantum devices that couple to electric fields. As a result, piezoelectric resonators have found significant use in recent experiments with solid-state qubits [8–10].

The resonant, capacitive coupling g between a piezoelectric mechanical resonator and a qubit is proportional to the zero-point electric field fluctuations of the resonator. As with other types of resonators, the strength of these fluctuations is inversely proportional to the square root of the mode volume, and $g \propto 1/\sqrt{V}$ [11]. Because the zero-point energy of a resonator does not depend on its volume, resonators with smaller volumes have larger zero-point energy densities and thus larger electric field fluctuations. Equivalently, for piezoelectric resonators, the effective *parallel RLC* circuit representing the resonator should have a high characteristic impedance $Z_c = \sqrt{L/C}$, where L and C are the inductance and capacitance of the circuit. The resulting coupling $g \propto \sqrt{Z_c}$. Surface acoustic waves (SAWs) [12,13] are mechanical modes that are naturally confined to surfaces and thus present an attractive

option for tightly confined resonant modes [5,14]. In part because of this promise and because they are relatively easy to fabricate and measure, recent research has focused on realizing the potential of SAW resonators for solid-state quantum information processing [11,15–26].

SAW resonators feature tight confinement in the spatial direction normal to the surface, and lateral confinement can occur through phononic bandgaps [27,28] and focusing electrodes [24,29–37]. Despite this progress, however, the zero-point electric field fluctuations of current SAW resonators are still not large enough for strong capacitive coupling to nanoscale qubits. For example, achieving strong coupling between a microwave resonator and a semiconductor quantum-dot qubit generally requires a characteristic impedance larger than 100Ω [38–40]. (We refer to such an impedance as “high” because it exceeds 50Ω , the most common impedance for microwave electronics.) High impedances such as these can be readily achieved with superconducting microwave resonators, but SAW resonators generally feature significantly lower impedance values of the order of $1\text{--}10 \Omega$ [19,41].

In this work, we demonstrate the creation of high-impedance SAW resonators. We fabricate gigahertz-frequency SAW resonators whose equivalent parallel *RLC* circuits have characteristic impedances exceeding 100Ω and quality factors of several thousand at millikelvin temperatures. We achieve such high impedance values through multiple strategies to confine the mode and boost the zero-point electric field fluctuations. We use lithium niobate, a strong piezoelectric material, as the substrate, and we use curved, highly reflective focusing mirrors to generate

*john.nichol@rochester.edu

a confined Gaussian mode, as well as the quasiconstant acoustic reflection periodicity geometry for the transducer [19,42] to mitigate coupling to bulk acoustic modes. These results underscore the potential of SAW resonators as key elements of hybrid quantum systems.

II. RESONATOR DESIGN AND FABRICATION

We optimize our SAW resonators for large characteristic impedance and low dissipation, balancing several competing effects. First, we use 128° Y-cut LiNbO_3 as a substrate. Because the characteristic impedance of the effective parallel RLC circuit representing the SAW resonator is proportional to the piezoelectric coupling, K^2 [43], we choose 128° Y-cut LiNbO_3 as a substrate for its relatively high K^2 . Second, we engineer the resonators themselves for small mode volumes. Mirrors for SAW resonators are generally thin metal electrodes or etched grooves in the substrate. The reflectivity per electrode or groove increases with the ratio of the thickness of the electrode or groove h to the SAW wavelength λ , and as the reflectivity increases, the mode volume decreases. Thus, we fabricate our resonators with relatively large h/λ . Our electrodes are electrically floating to take advantage of regeneration reflection [12]. We also fabricate small interdigital transducers (IDTs) to minimize the mode volume. The small size also reduces the IDT capacitance, as discussed further below.

Although thick electrodes enable small mode volumes, they also increase the coupling between surface and bulk modes, which increases dissipation [11]. To mitigate this effect, we use the quasiconstant acoustic reflection periodicity (QARP) geometry [19,42] for the IDT. Conventional SAW resonators feature a relatively large space between the electrodes of the IDT and those of the mirrors. The QARP geometry eliminates this gap such that the electrodes have an approximately constant spacing over the length of the resonator to ensure a nearly constant effective wave speed for SAWs along the direction of propagation. Another drawback of increased electrode thickness is the significant mass loading of the resonator, which can reduce effective SAW velocity and, thus, the frequency of the resonator. To compensate for this effect, we adjust the periodicity of the electrodes to ensure that the desired resonance is in the center of the mirror stop band [36,44].

A natural approach to confine the mode in the transverse direction is to reduce the length of the electrodes. For flat mirrors, however, reducing their length increases diffraction losses [5]. To mitigate this effect, we design our mirrors to focus SAWs [29–32] and create a Gaussian mode [24,35,45] with a relatively small beam waist. (Empirically, we find that a beam waist of 2λ enables small mode volumes with relatively large quality factors. Larger beam waists increase the mode volume, and smaller beam waists require mirrors with larger curvature, which creates additional challenges due to the anisotropy of the

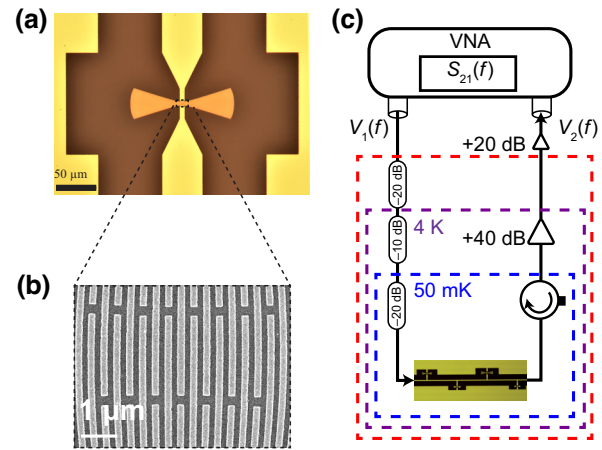


FIG. 1. Gaussian SAW resonator and measurement setup. (a) Optical micrograph of a Gaussian SAW resonator with contact pads for probe tips. (b) Scanning electron micrograph of the transducer of a typical Gaussian SAW resonator. (c) Cryogenic measurement setup. Using a vector network analyzer (VNA), we measure the transmission as a function of frequency $S_{21}(f)$ through a Nb coplanar waveguide with multiple SAW resonators attached in “hanger” mode [46,47].

substrate. Here, the wavelength $\lambda \approx 1 \mu\text{m}$ at 4 GHz.) We design our mirrors taking into account the simulated angle-dependent group velocity of 128° Y-cut LiNbO_3 [44]. To avoid exciting higher-order Gaussian modes, we apodize the transducer electrodes such that their length is 0.8 times the beam waist of the Gaussian mode. We empirically find that this geometry results in minimal coupling to higher-order modes. We fabricate the resonators using electron beam lithography, ultra-high-vacuum electron beam evaporation of Al, and liftoff. Figures 1(a) and 1(b) show images of a typical Gaussian SAW resonator.

III. ROOM-TEMPERATURE CHARACTERIZATION

SAW resonators function well at room temperature. We take advantage of this property to perform a thorough electrical characterization of the SAW resonators at room temperature. We use a custom probe station with microwave probe tips and a vector network analyzer to measure the transmission through the IDT. To facilitate this measurement, we fabricate SAW resonators with large contact pads for both the IDT and ground. Figure 2(b) shows a typical resonance observed at room temperature.

SAW resonators are commonly modeled using the Butterworth-Van Dyke (BVD) circuit model, which consists of a series RLC circuit in parallel with the IDT capacitance [13]. Such a circuit naturally models the electrical admittance associated with SAW propagation. The BVD model is not the only way to model piezoelectric resonators. In fact, there exist mappings between the BVD

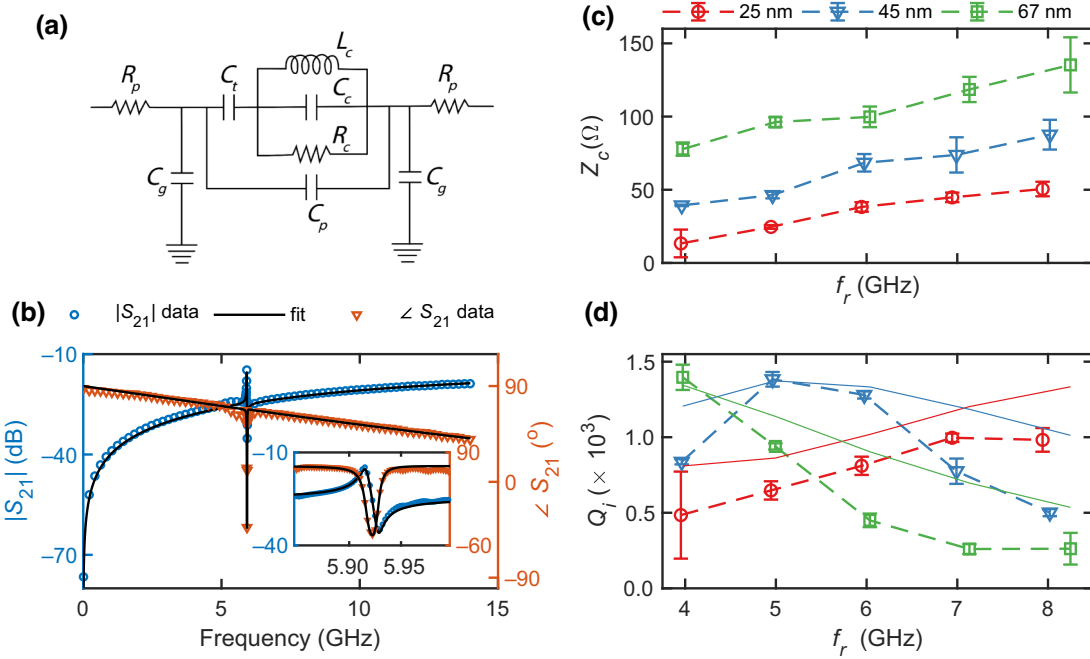


FIG. 2. Room-temperature characterization of SAW resonators. (a) The effective circuit used to model the response of the SAW resonators. (b) Measured magnitude and phase of the transmission through the transducer of a 6-GHz resonator and fit. (c),(d) Extracted characteristic impedance and quality factor values for resonators with frequencies between 4 and 8 GHz. For each frequency, five different resonators are characterized, and their average parameters are indicated. The error bars are the range of the fit values. The resonators have Al electrodes of different thicknesses. Theoretical predictions for the quality factors are displayed with solid lines in (d).

model and a variety of other effective circuits, including a parallel RLC model [43,48]. The parallel RLC model consists of a parallel RLC circuit in series with the IDT capacitance [Fig. 2(a)]. This model emphasizes the impedance of the resonator instead of its admittance. In the quantum regime, this circuit can be interpreted as a quantum harmonic oscillator in series with a coupling capacitance from the IDT. The main advantage of this model over the traditional BVD model is that the displacement of this oscillator can be identified with the voltage across the IDT pads. In the high-quality-factor limit, the zero-point voltage fluctuations are proportional to the resonator's "characteristic impedance" $Z_c = \sqrt{L_c/C_c}$ [49].

When modeling the transmission through these devices, we also include stray capacitances between the contact pads and ground (C_g), as well as between the contact pads themselves (C_p) [Fig. 2(a)]. We need these elements to accurately model our data because the capacitance of the IDT itself is only a few femtofarads for our devices, and the large contact pads and probe tips can easily add comparable or larger capacitances to the circuit. We also add a contact resistance (R_p) associated with the probe tips [19]. Using the model of Fig. 2(a), we calculate the transmission versus frequency as a function of the circuit parameters, and we fit the data to extract the parameters.

Fitting our data to such a complex model poses multiple challenges, including determining the large stray capacitances, which can overwhelm the transducer capacitance. As described further in the Supplemental Material [44], we solve this challenge by fabricating a series of control devices for each resonator. One control device has the same contact pads but no IDT or mirror electrodes. The other control device has contact pads and IDT electrodes but no mirror electrodes. Using finite-element simulations of the device geometry to produce initial guesses for the stray capacitances, we fit the data from the first control device (contact pads only, no IDT or mirrors) to extract C_p , and we determine C_g through finite-element simulations. We fit the data from the second control device (contact pads and IDT, but no mirrors) to extract the IDT capacitance, and we fit the full devices to extract the resonator parameters (Fig. 2). We have confirmed that our fitting results do not change significantly if the initial values of C_p and C_g are changed by $\pm 25\%$ from the values predicted by finite-element simulation. As discussed further below, we also corroborate our fit results with three-dimensional finite-element simulations of microwave transmission through the resonators.

Figure 2(b) displays the transmission through a typical 6-GHz resonator with 200 45-nm-thick Al electrodes in Gaussian mirrors on either side of the transducer and

our fits. Figure 2(c) displays our extracted impedance values for resonators with frequencies between 4 and 8 GHz with different electrode thicknesses. For each frequency, we measure five nominally identical resonators and plot the average values. We observe that as the frequency of the resonator increases, the effective electrical impedance increases, consistent with our expectation that the mode volume decreases with the acoustic wavelength. We also observe that for a fixed frequency, as the electrode thickness increases, the impedance increases, consistent with our expectation that thicker electrodes confine the mode more effectively. We achieve a maximum impedance well above 100 Ω for resonators in the frequency range tested.

Typical values of the IDT capacitance, C_t , in our devices are about 5–10 fF. Typical stray capacitance values are $C_p \sim 10$ fF and $C_g \sim 70$ fF [44]. Future hybrid quantum devices using capacitive coupling to high-impedance SAW resonators will require low-capacitance wiring with $C_p, C_g \ll C_t$. The most significant contribution to the stray capacitance in our devices comes from the large probe-tip contact pads, which can be eliminated in future devices. Without the large contact pads, we expect that low-capacitance wiring to other solid-state systems can easily be achieved [50].

Figure 2(d) displays the extracted internal quality factors $Q_i = R_c \sqrt{C_c/L_c} = R_c/Z_c$. For 25-nm-thick electrodes, we observe that the quality factor increases with frequency. However, for 67-nm-thick electrodes, we observe that the quality factor decreases with frequency, and for 45-nm-thick electrodes, we observe a maximum in the quality factor around 5 GHz, and then a reduction in the quality factor at higher frequencies. We can understand these trends by considering the competition between loss through the mirrors, which decreases with h/λ , and bulk dissipation, which increases with h/λ [11]. Figure 2(d) also displays theoretical predictions calculated using expressions for grooved, flat resonators [11] for the total quality factor considering mirror loss, bulk loss, and material loss. The only free parameters in our calculations are a scaling factor (0.2) for the predicted reflectivity per electrode [12], to account for the angle-dependent piezoelectric coupling in the substrate, and a quality factor associated with material loss [44]. The relatively good agreement between our data and the predictions corroborates the interpretation of the different trends in the data.

We have checked that our various strategies to confine the mode have the desired effect (Fig. 3). For example, increasing the number of electrodes in the IDT for a fixed thickness should increase the mode volume and thus decrease the impedance, in agreement with our observations [Fig. 3(a)]. We have also fabricated resonators with the standard electrode periodicity as opposed to the QARP geometry. In these cases, we find reduced impedance values and quality factors, presumably due to increased coupling to bulk modes [Fig. 3(a)]. Finally, we have fabricated

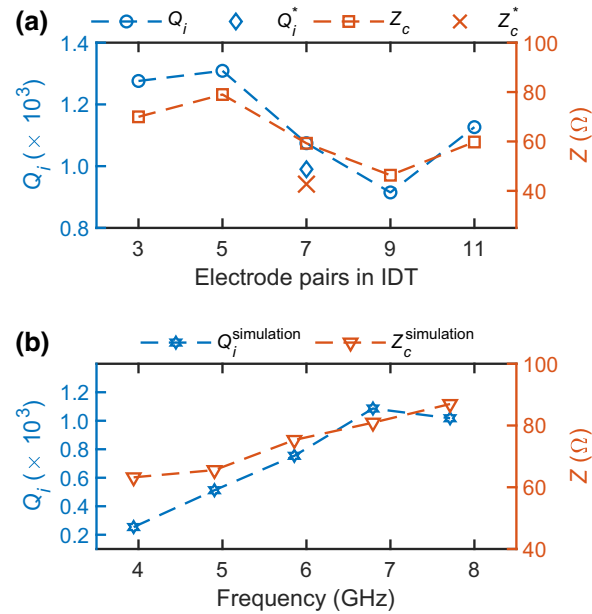


FIG. 3. Comparison of different resonator types. (a) Comparison of 6-GHz Gaussian resonators with different numbers of electrodes in the IDT. For IDTs with seven pairs of electrodes, data for non-QARP Gaussian resonators, indicated by an $*$, are also shown. Electrodes are 45 nm thick. (b) Results of finite-element simulations of SAW resonators with 45-nm-thick Al electrodes and seven pairs of electrodes in the IDT.

SAW resonators with flat mirrors and similar sizes to the Gaussian resonators. The smallest flat resonators (beam width equal to 4λ) are apparently not effective in confining a single mode, because multiple modes spaced by less than the free spectral range are visible [44]. For larger flat resonators (beam width equal to 42λ), we observe single modes with quality factors significantly lower than the Gaussian resonators, likely because of increased diffraction loss [44]. Note that a beam width of 42λ is significantly smaller than other flat SAW resonators reported in the literature, which are typically of the order of hundreds of wavelengths wide [19].

We have also conducted three-dimensional finite-element simulations in COMSOL Multiphysics [Fig. 3(b)]. As described further in the Supplemental Material [44], we simulate the microwave transmission through the transducer for SAW devices with different resonance frequencies. For each SAW resonator, we fit the simulated transmission to the circuit of Fig. 2(a), except that we do not include any stray capacitances or contact resistance, because the simulation contains no probe tips or contact pads. Figure 3(b) shows the quality factors and impedance values from these fits. The simulated impedance increases with the frequency, in quantitative agreement with our measurements. The quality factor reaches a maximum near 7 GHz. This trend agrees qualitatively with our data, which indicate that the quality factor goes through a maximum

in this frequency range. While the measured devices have 200 electrodes in each mirror, the simulated devices have only 50 electrodes to reduce the computational resources required. We hypothesize that energy loss through the mirrors reduces the quality factor for low-frequency devices more significantly in our simulations than in the actual devices. It could also be that the specific details of the finite-element simulation, such as the mesh density, which is constrained by our computational resources, contribute to an inaccurate determination of the quality factor.

These measurements and simulations highlight the potential of Gaussian SAW resonators for small mode volumes and correspondingly high impedance values. Based on our finite-element simulations, we expect that our mode volumes are of the order of a few cubic micrometers. For our highest-frequency resonators, the mode volume is significantly smaller than can be achieved with phononic-crystal mirrors, for example [28]. Moreover, our approach also relies on a simple, intuitive analogy with free-space optics to confine the mode. The ability to create resonators with effective electrical impedances well above 50Ω opens the door to strong coupling to various quantum systems.

IV. CRYOGENIC CHARACTERIZATION

Having confirmed the potential for small mode volumes at high frequencies at room temperature, we characterize the resonators at millikelvin temperatures in a dilution

refrigerator. We fabricated a niobium coplanar waveguide transmission line on the LiNbO_3 substrate, and then we coupled multiple resonators of different frequencies to the waveguide. One side of each IDT is galvanically connected to the center conductor, and the other side is galvanically connected to the ground plane. In this configuration, we measure the resonators in “hanger” mode [46] [Fig. 1(c)].

Figure 4(a) shows a typical resonance curve and fit associated with a 6-GHz resonator with 45-nm-thick Al electrodes. Because extracting the effective circuit parameters (as we did at room temperature) relies critically on accurate calibration of the entire microwave circuit, and because of the challenges associated with calibrating the microwave wiring in a cryostat, we cannot directly determine the impedance of the resonators at low temperature. Instead, we focus on measuring the resonator quality factor at low temperature [46]. Previous studies have suggested that some piezoelectric coupling coefficients in LiNbO_3 do not depend very strongly on temperature [51,52], so we hypothesize that the impedance does not change significantly on cooling to cryogenic temperatures. We observe only slight frequency shifts (approximately 90 MHz) when cooling down the resonators. These shifts may result from thermal contraction or a decrease in the dielectric constant, which would affect the transducer capacitance. Nevertheless, the minimal frequency shifts we observe suggest that the effective inductance and capacitance of the resonator, and thus its impedance, do not change significantly upon

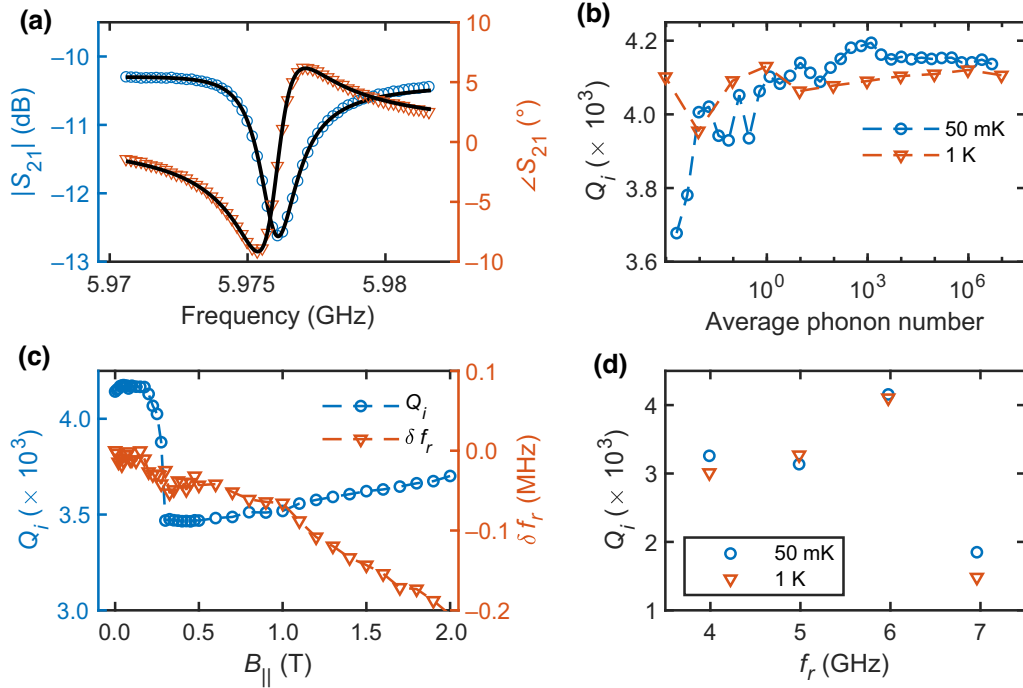


FIG. 4. Millikelvin characterization of SAW resonators. (a) Magnitude and phase of the transmission through the coplanar waveguide near 6 GHz and fit for the 6-GHz resonator. (b) Internal quality factors versus average phonon number for the 6-GHz resonator. (c) Internal quality factor and change in resonance frequency compared to zero magnetic field value ($\delta f_r = f_r(B_{||}) - f_r(0)$) versus in-plane magnetic field for the 6-GHz resonator. (d) Internal quality factor versus resonator frequency. Data for (a), (c), and (d) were taken in the large phonon-number limit.

cooling. Future studies can also confirm this by measuring the frequency difference between the admittance and impedance maxima of the resonator at different temperatures [43].

We measure the transmission through the coplanar waveguide and fit the data near each resonance to a standard resonator model, which features the resonance frequency and internal and coupling quality factors (Q_i and Q_c) as fit parameters [46]. Figure 4(b) shows the extracted internal and coupling quality factors for the 6-GHz resonator at different average phonon numbers calculated as $\langle n \rangle = Q_c/\omega_r [Q_i/(Q_i + Q_c)]^2 (P_{\text{in}}/\hbar\omega_r)$ [53] where \hbar is the reduced Planck constant, $\omega_r = 2\pi f_r$, and P_{in} is the input power. We observe that the quality factor increases weakly with phonon number at both 50 mK and 1 K. This behavior suggests the saturation of two-level systems [17], as is often seen with superconducting microwave resonators. We also plot the internal quality factor and change in resonance frequency versus the in-plane magnetic field [Fig. 4(c)]. We observe that the internal quality factor drops by a small amount near a few hundred militesla. This behavior is consistent across all resonators we measure, and we hypothesize that this reduction occurs when the Al electrodes become nonsuperconducting. We expect a much higher critical field for the Nb coplanar waveguide. [We also observed slight irreversible downward shifts (~ 5 MHz) in the resonator frequencies on the first field sweep. See the Supplemental Material for more details [44].] Despite this small drop, the resonator, which is expected to have an impedance around 100 Ω based on room-temperature measurements, maintains a quality factor above 3000 until a magnetic field of 2 T, an encouraging prospect for compatibility with devices such as spin qubits, which often require magnetic fields for their operation.

Finally, we plot the internal quality factor for different resonators at both 50 mK and 1 K at zero magnetic field [Fig. 4(d)]. Resonators with frequencies between 4 and 6 GHz have internal quality factors of several thousand at millikelvin temperatures. As above, with the room-temperature resonators, we observe that the quality factor decreases for the highest-frequency resonators. In contrast to the room-temperature devices, the 6 GHz resonator maintains a relatively high quality factor, while the 8-GHz resonator has a quality factor that was too low to measure. These differences may result from variations in fabrication conditions between devices. (The cryogenic devices were made during a different fabrication run and with a different process than the room-temperature devices [44].)

V. OUTLOOK

We have demonstrated that through a combination of design choices, we can create SAW resonators with high impedance values and quality factors at millikelvin temperatures. The performance of the SAW resonators

described here is already sufficient to enable strong coupling between an individual electron in a quantum dot [54–56] and a single phonon [44]. To estimate the charge-phonon coupling rate possible with our current devices, consider the results of Ref. [56], where a charge-photon coupling rate $g_c/(2\pi) = 154$ MHz was measured between a 5-GHz, 1- $k\Omega$ superconducting resonator and a single electron in a double dot with a corresponding charge-qubit dephasing rate $\gamma_c/(2\pi) = 28.3$ MHz. Because the charge coupling rate scales as the square root of the impedance, and taking a typical SAW-resonator impedance of 100 Ω , we would expect a charge-phonon coupling of $g_{\text{ph}}/(2\pi) = \sqrt{1/10}g_c/(2\pi) = 47$ MHz, which is still larger than the charge-qubit dephasing rate. Taking a typical SAW-resonator quality factor of 3000, the phonon decay rate is expected to be $\kappa_{\text{ph}}/(2\pi) = f/Q \sim 2$ MHz, which is less than $g_{\text{ph}}/(2\pi)$. In order to achieve strong spin-phonon coupling, even larger impedances will be required. Alternatively, a high-impedance superconducting microwave resonator could be used as an intermediary between a mechanical resonator and spin qubit to boost the coupling, similar to the case where two qubits coupled to the same resonator experience an effective coupling [57].

A major technical challenge to the integration of mechanical resonators and quantum-dot devices is to suppress excess capacitance from the resonator-qubit wiring. Reducing stray capacitance is also a challenge in coupling quantum dots to superconducting resonators. Encouragingly, however, low-capacitance resonators have already been successfully integrated with quantum dots [50,56]. Another technical challenge involves the integration of dissimilar materials, such as LiNbO_3 with spin-qubit materials like Si/SiGe or GaAs. We envision overcoming this challenge with flip-chip integration techniques, which have been successfully demonstrated with various qubit platforms [58,59]. Lithium niobate thin films can also be bonded to other materials such as silicon [60].

Beyond semiconductor qubits, we expect that the high-impedance SAW resonators presented here will also find use in other platforms. Capacitive coupling between superconducting qubits and SAW resonators have enabled exploring dissipation-mediated state preparation [61], mode-selective coupling [18], strong-dispersive couplings [21], and quantum cavity acoustodynamics [17]. We envision that high-impedance resonators can enable further research in these directions. High-impedance SAW resonators may also enable coupling to other types of voltage-tunable spin qubits, such as self-assembled quantum dots [62,63]. For all of these applications, a detailed assessment of the dissipation mechanisms will be helpful for further progress toward increasing the impedance and reducing the dissipation. Our measurements show a relatively small reduction in quality factor when the Al electrodes become nonsuperconducting, suggesting that electrical resistivity in the transducer is not the dominant loss mechanism

at low temperatures. Given the reduction in quality factor with frequency observed in Fig. 2, we hypothesize that coupling to bulk modes is a limiting mechanism, potentially resulting from the details of the electrode curvature. In addition, the metal electrodes in the transducer also likely have a significant impact on the reflections in the cavity. Exploring, for example, strategies to minimize reflection associated with the transducer, such as using a split-finger geometry, could also be worthwhile.

Altogether, our results emphasize the potential of SAW resonators for integration in future hybrid architectures. Just as with superconducting microwave resonators, whose compatibility with a variety of quantum devices is enhanced by the potential of high impedance and large vacuum electric field fluctuations, the ability to engineer confined acoustic modes with low dissipation opens the door to exciting applications for hybrid quantum architectures.

The processed data are available at [64]. The raw data are available from the corresponding author upon reasonable request.

ACKNOWLEDGMENTS

This work was sponsored by the Army Research Office, grant number W911NF-19-1-0167, and the Office of Naval Research, grant number N00014-20-1-2424. The views and conclusions contained in this document are those of the authors and should not be interpreted as representing the official policies, either expressed or implied, of the Army Research Office, the Office of Naval Research, or the U.S. Government. The U.S. Government is authorized to reproduce and distribute reprints for government purposes notwithstanding any copyright notation herein.

- [1] S. Bravyi, O. Dial, J. M. Gambetta, D. Gil, and Z. Nazario, The future of quantum computing with superconducting qubits, *J. Appl. Phys.* **132**, 160902 (2022).
- [2] D. Awschalom, K. K. Berggren, H. Bernien, S. Bhave, L. D. Carr, P. Davids, S. E. Economou, D. Englund, A. Faraon, and M. Fejer, *et al.*, Development of quantum interconnects (quics) for next-generation information technologies, *PRX Quantum* **2**, 017002 (2021).
- [3] M. Aspelmeyer, T. Jennewein, M. Pfennigbauer, W. Leeb, and A. Zeilinger, Long-distance quantum communication with entangled photons using satellites, *IEEE J. Sel. Top. Quantum Electron.* **9**, 1541 (2003).
- [4] G. Kurizki, P. Bertet, Y. Kubo, K. Mølmer, D. Petrosyan, P. Rabl, and J. Schmiedmayer, Quantum technologies with hybrid systems, *Proc. Natl. Acad. Sci.* **112**, 3866 (2015).
- [5] T. Aref, P. Delsing, M. K. Ekström, A. F. Kockum, M. V. Gustafsson, G. Johansson, P. J. Leek, E. Magnusson, and R. Manenti, in *Superconducting Devices in Quantum Optics*, edited by R. Hadfield and G. Johansson. Quantum Science and Technology (Springer, Cham, 2016).
- [6] Y. Chu and S. Gröblacher, A perspective on hybrid quantum opto- and electromechanical systems, *Appl. Phys. Lett.* **117**, 150503 (2020).
- [7] A. Clerk, K. Lehnert, P. Bertet, J. Petta, and Y. Nakamura, Hybrid quantum systems with circuit quantum electrodynamics, *Nat. Phys.* **16**, 257 (2020).
- [8] A. D. O'Connell, M. Hofheinz, M. Ansmann, R. C. Bialczak, M. Lenander, E. Lucero, M. Neeley, D. Sank, H. Wang, and M. Weides, *et al.*, Quantum ground state and single-phonon control of a mechanical resonator, *Nature* **464**, 697 (2010).
- [9] Y. Chu, P. Kharel, W. H. Renninger, L. D. Burkhardt, L. Frunzio, P. T. Rakich, and R. J. Schoelkopf, Quantum acoustics with superconducting qubits, *Science* **358**, 199 (2017).
- [10] M. Mirhosseini, A. Sipahigil, M. Kalaee, and O. Painter, Superconducting qubit to optical photon transduction, *Nature* **588**, 599 (2020).
- [11] M. J. A. Schuetz, E. M. Kessler, G. Giedke, L. M. K. Vandersypen, M. D. Lukin, and J. I. Cirac, Universal quantum transducers based on surface acoustic waves, *Phys. Rev. X* **5**, 031031 (2015).
- [12] S. Datta, *Surface Acoustic Wave Devices* (Prentice-Hall, Englewood Cliffs, New Jersey, 1986).
- [13] D. Morgan, *Surface Acoustic Wave Filters: With Applications to Electronic Communications and Signal Processing* (Academic Press, Amsterdam, 2010).
- [14] P. Delsing, A. N. Cleland, M. J. Schuetz, J. Knörzer, G. Giedke, J. I. Cirac, K. Srinivasan, M. Wu, K. C. Balram, and C. Bäuerle, *et al.*, The 2019 surface acoustic waves roadmap, *J. Phys. D: Appl. Phys.* **52**, 353001 (2019).
- [15] M. V. Gustafsson, T. Aref, A. F. Kockum, M. K. Ekström, G. Johansson, and P. Delsing, Propagating phonons coupled to an artificial atom, *Science* **346**, 207 (2014).
- [16] D. A. Golter, T. Oo, M. Amezcuia, K. A. Stewart, and H. Wang, Optomechanical quantum control of a nitrogen-vacancy center in diamond, *Phys. Rev. Lett.* **116**, 143602 (2016).
- [17] R. Manenti, M. Peterer, A. Nersisyan, E. Magnusson, A. Patterson, and P. Leek, Surface acoustic wave resonators in the quantum regime, *Phys. Rev. B* **93**, 041411 (2016).
- [18] B. A. Moores, L. R. Sletten, J. J. Viennot, and K. Lehnert, Cavity quantum acoustic device in the multimode strong coupling regime, *Phys. Rev. Lett.* **120**, 227701 (2018).
- [19] K. J. Satzinger, Y. Zhong, H.-S. Chang, G. A. Peairs, A. Bienfait, M.-H. Chou, A. Cleland, C. R. Conner, É. Dumur, and J. Grebel, *et al.*, Quantum control of surface acoustic-wave phonons, *Nature* **563**, 661 (2018).
- [20] A. Bienfait, K. J. Satzinger, Y. Zhong, H.-S. Chang, M.-H. Chou, C. R. Conner, É. Dumur, J. Grebel, G. A. Peairs, and R. G. Povey, *et al.*, Phonon-mediated quantum state transfer and remote qubit entanglement, *Science* **364**, 368 (2019).
- [21] L. R. Sletten, B. A. Moores, J. J. Viennot, and K. W. Lehnert, Resolving phonon Fock states in a multimode cavity with a double-slit qubit, *Phys. Rev. X* **9**, 021056 (2019).
- [22] A. Bienfait, Y. Zhong, H.-S. Chang, M.-H. Chou, C. R. Conner, É. Dumur, J. Grebel, G. A. Peairs, R. G. Povey, and K. J. Satzinger, *et al.*, Quantum erasure using entangled surface acoustic phonons, *Phys. Rev. X* **10**, 021055 (2020).
- [23] A. Noguchi, R. Yamazaki, Y. Tabuchi, and Y. Nakamura, Qubit-assisted transduction for a detection of surface

acoustic waves near the quantum limit, *Phys. Rev. Lett.* **119**, 180505 (2017).

[24] S. J. Whiteley, G. Wolfowicz, C. P. Anderson, A. Bourassa, H. Ma, M. Ye, G. Koolstra, K. J. Satzinger, M. V. Holt, and F. J. Heremans, *et al.*, Spin–phonon interactions in silicon carbide addressed by Gaussian acoustics, *Nat. Phys.* **15**, 490 (2019).

[25] S. Maity, L. Shao, S. Bogdanović, S. Meesala, Y.-I. Sohn, N. Sinclair, B. Pingault, M. Chalupnik, C. Chia, and L. Zheng, *et al.*, Coherent acoustic control of a single silicon vacancy spin in diamond, *Nat. Commun.* **11**, 193 (2020).

[26] S. Maity, B. Pingault, G. Joe, M. Chalupnik, D. Assumpção, E. Cornell, L. Shao, and M. Lončar, Mechanical control of a single nuclear spin, *Phys. Rev. X* **12**, 011056 (2022).

[27] S. Benchabane, A. Khelif, J.-Y. Rauch, L. Robert, and V. Laude, Evidence for complete surface wave band gap in a piezoelectric phononic crystal, *Phys. Rev. E* **73**, 065601 (2006).

[28] L. Shao, S. Maity, L. Zheng, L. Wu, A. Shams-Ansari, Y.-I. Sohn, E. Puma, M. Gadalla, M. Zhang, and C. Wang, *et al.*, Phononic band structure engineering for high- Q gigahertz surface acoustic wave resonators on lithium niobate, *Phys. Rev. Appl.* **12**, 014022 (2019).

[29] M. S. Kharusi and G. W. Farnell, On diffraction and focusing in anisotropic crystals, *Proc. IEEE* **60**, 945 (1972).

[30] J. Z. Wilcox and R. E. Brooks, Time-Fourier transform by a focusing array of phased surface acoustic wave transducers, *J. Appl. Phys.* **58**, 1148 (1985).

[31] J. Z. Wilcox and R. E. Brooks, Frequency-dependent beam steering by a focusing array of surface acoustic wave transducers: Experiment, *J. Appl. Phys.* **58**, 1160 (1985).

[32] M. de Lima Jr, F. Alsina, W. Seidel, and P. Santos, Focusing of surface-acoustic-wave fields on (100) GaAs surfaces, *J. Appl. Phys.* **94**, 7848 (2003).

[33] V. Laude, D. Gérard, N. Khelfaoui, C. F. Jerez-Hanckes, S. Benchabane, and A. Khelif, Subwavelength focusing of surface acoustic waves generated by an annular interdigital transducer, *Appl. Phys. Lett.* **92**, 094104 (2008).

[34] A. Vainsencher, K. Satzinger, G. Peairs, and A. Cleland, Bi-directional conversion between microwave and optical frequencies in a piezoelectric optomechanical device, *Appl. Phys. Lett.* **109**, 033107 (2016).

[35] M. E. Msall and P. V. Santos, Focusing surface-acoustic-wave microcavities on GaAs, *Phys. Rev. Appl.* **13**, 014037 (2020).

[36] R. A. DeCrescent, Z. Wang, P. Imany, R. C. Boutelle, C. A. McDonald, T. Autry, J. D. Teufel, S. W. Nam, R. P. Mirin, and K. L. Silverman, Large single-phonon optomechanical coupling between quantum dots and tightly confined surface acoustic waves in the quantum regime, *Phys. Rev. Appl.* **18**, 034067 (2022).

[37] P. Imany, Z. Wang, R. A. DeCrescent, R. C. Boutelle, C. A. McDonald, T. Autry, S. Berweger, P. Kabos, S. W. Nam, and R. P. Mirin, *et al.*, Quantum phase modulation with acoustic cavities and quantum dots, *Optica* **9**, 501 (2022).

[38] X. Mi, M. Benito, S. Putz, D. M. Zajac, J. M. Taylor, G. Burkard, and J. R. Petta, A coherent spin-photon interface in silicon, *Nature* **555**, 599 (2018).

[39] N. Samkharadze, G. Zheng, N. Kalhor, D. Brousse, A. Sammak, U. C. Mendes, A. Blais, G. Scappucci, and L. M. K. Vandersypen, Strong spin-photon coupling in silicon, *Science* **359**, 1123 (2018).

[40] A. J. Landig, J. V. Koski, P. Scarlino, U. C. Mendes, A. Blais, C. Reichl, W. Wegscheider, A. Wallraff, K. Ensslin, and T. Ihn, Coherent spin-photon coupling using a resonant exchange qubit, *Nature* **560**, 179 (2018).

[41] The resonator of Ref. [19] is optimized for inductive coupling to a superconducting qubit, not capacitive coupling. For a fixed transducer capacitance, inductive coupling improves as the mode volume decreases.

[42] Y. Ebata, in *IEEE 1988 Ultrasonics Symposium Proceedings* (IEEE, Chicago, 1988), p. 91.

[43] K. J. Satzinger, Ph.D. thesis, University of California, Santa Barbara, 2018.

[44] See Supplemental Material at <http://link.aps.org/supplemental/10.1103/PhysRevApplied.21.014010> for the details on design, fabrication, and characterization of SAW resonators.

[45] R. O'Rorke, A. Winkler, D. Collins, and Y. Ai, Slowness curve surface acoustic wave transducers for optimized acoustic streaming, *RSC Adv.* **10**, 11582 (2020).

[46] S. Probst, F. Song, P. A. Bushev, A. V. Ustinov, and M. Weides, Efficient and robust analysis of complex scattering data under noise in microwave resonators, *Rev. Sci. Instrum.* **86**, 024706 (2015).

[47] C. R. H. McRae, H. Wang, J. Gao, M. R. Visser, T. Brecht, A. Dunsworth, D. P. Pappas, and J. Mutus, Materials loss measurements using superconducting microwave resonators, *Rev. Sci. Instrum.* **91**, 091101 (2020).

[48] E. A. Wollack, A. Y. Cleland, P. Arrangoiz-Arriola, T. P. McKenna, R. G. Gruenke, R. N. Patel, W. Jiang, C. J. Sarabalis, and A. H. Safavi-Naeini, Loss channels affecting lithium niobate phononic crystal resonators at cryogenic temperature, *Appl. Phys. Lett.* **118**, 123501 (2021).

[49] U. Vool and M. Devoret, Introduction to quantum electromagnetic circuits, *Int. J. Circuit Theory Appl.* **45**, 897 (2017).

[50] P. Harvey-Collard, J. Dijkema, G. Zheng, A. Sammak, G. Scappucci, and L. M. Vandersypen, Coherent spin–spin coupling mediated by virtual microwave photons, *Phys. Rev. X* **12**, 021026 (2022).

[51] F. Chen, C. Jiang, F. Yu, X. Cheng, and X. Zhao, Investigation of electro-elastic properties for In single crystals at low temperature, *Appl. Sci.* **11**, 7374 (2021).

[52] M. S. Islam and J. Beamish, Piezoelectric creep in LiNbO₃, PMN-PT and PZT-5A at low temperatures, *J. Appl. Phys.* **126**, 204101 (2019).

[53] C. X. Yu, S. Zihlmann, G. Troncoso Fernández-Bada, J.-L. Thomassin, F. Gustavo, É. Dumur, and R. Maurand, Magnetic field resilient high kinetic inductance superconducting niobium nitride coplanar waveguide resonators, *Appl. Phys. Lett.* **118**, 054001 (2021).

[54] X. Mi, J. Cady, D. Zajac, P. Deelman, and J. R. Petta, Strong coupling of a single electron in silicon to a microwave photon, *Science* **355**, 156 (2017).

[55] A. Stockklauser, P. Scarlino, J. V. Koski, S. Gasparinetti, C. K. Andersen, C. Reichl, W. Wegscheider, T. Ihn,

K. Ensslin, and A. Wallraff, Strong coupling cavity QED with gate-defined double quantum dots enabled by a high impedance resonator, *Phys. Rev. X* **7**, 011030 (2017).

[56] P. Scarlino, J. H. Ungerer, D. J. van Woerkom, M. Mancini, P. Stano, C. Müller, A. J. Landig, J. V. Koski, C. Reichl, and W. Wegscheider, *et al.*, In situ tuning of the electric-dipole strength of a double-dot charge qubit: Charge-noise protection and ultrastrong coupling, *Phys. Rev. X* **12**, 031004 (2022).

[57] J. Majer, J. Chow, J. Gambetta, J. Koch, B. Johnson, J. Schreier, L. Frunzio, D. Schuster, A. A. Houck, and A. Wallraff, *et al.*, Coupling superconducting qubits via a cavity bus, *Nature* **449**, 443 (2007).

[58] K. Satzinger, C. Conner, A. Bienfait, H.-S. Chang, M.-H. Chou, A. Cleland, É. Dumur, J. Grebel, G. Peairs, and R. Povey, *et al.*, Simple non-galvanic flip-chip integration method for hybrid quantum systems, *Appl. Phys. Lett.* **114**, 173501 (2019).

[59] N. Holman, D. Rosenberg, D. Yost, J. Yoder, R. Das, W. D. Oliver, R. McDermott, and M. Eriksson, 3D integration and measurement of a semiconductor double quantum dot with a high-impedance tin resonator, *npj Quantum Inf.* **7**, 137 (2021).

[60] T. Luschmann, A. Jung, S. Geprägs, F. X. Haslbeck, A. Marx, S. Filipp, S. Gröblacher, R. Gross, and H. Huebl, Surface acoustic wave resonators on thin film piezoelectric substrates in the quantum regime, *Mater. Quantum Technol.* **3**, 021001 (2023).

[61] J. Kitzman, J. Lane, C. Undershute, P. Harrington, N. Bey-sengulov, C. Mikolas, K. Murch, and J. Pollanen, Phononic bath engineering of a superconducting qubit, *Nat. Commun.* **14**, 3910 (2023).

[62] Y. Tsuchimoto, P. Knüppel, A. Delteil, Z. Sun, M. Kroner, and A. Imamoğlu, Proposal for a quantum interface between photonic and superconducting qubits, *Phys. Rev. B* **96**, 165312 (2017).

[63] Y. Tsuchimoto and M. Kroner, Low-loss high-impedance circuit for quantum transduction between optical and microwave photons, *Mater. Quantum Technol.* **2**, 025001 (2022).

[64] <https://doi.org/10.5281/zenodo.8060648>

[65] L. Kouwenhoven, D. G. Austing, and S. Tarucha, Few-electron quantum dots, *Rep. Prog. Phys.* **64**, 701 (2001).

Correction: The order of authors has been modified.